Search for the Decay $\mu^+ \to e^+ + \gamma$*

SHERWOOD PARKER, HERBERT L. ANDERSON, AND CHARLES REY

The Enrico Fermi Institute for Nuclear Studies and The Department of Physics,
The University of Chicago, Chicago, Illinois

(Received 26 August 1963)

A search has been conducted for the decay $\mu^+ \to e^+ + \gamma$ using spark chambers, scintillators, and fast oscilloscopes. The number of stopped pions, 7.39×10^9, and the detection efficiency of the apparatus for $\mu \to e + \gamma$ events, 3.9%, would predict the detection of 3 events for a branching ratio of 10^{-8}. No evidence for the existence of this decay was found. The distribution in range of the e^+ in graphite, and of the (e, γ) angle for the events found near 180° was consistent with that expected from $\mu^+ \to e^+ + \nu + \bar{\nu} + \gamma$. The probability of finding the observed distribution was calculated to be greatest for an assumed $\mu \to e + \gamma$ branching ratio of zero. This probability drops below 50% of this value if the branching ratio is 0.6×10^{-8}, and below 10% for 2.2×10^{-8}.

I. INTRODUCTION

EFFORTS to detect a neutrinoless conversion of a muon into an electron by any of the processes $\mu \to e + \gamma$,[1] $\mu \to 3e$,[2] and $\mu + \mathfrak{N} - e + \mathfrak{N}$[3] have been uniformly unsuccessful even though many attempts of increasing power have been made over the past fifteen years beginning with the initial work of Hincks and Pontecorvo. To forbid these neutrinoless $\mu \to e$ processes within the framework of the universal $V-A$ theory of weak interactions, specific restrictions have been imposed: (a) that the weak interaction takes place only through a singly charged current,[4] and (b) that the neutrino associated with the muon is different from that associated with the electron.[5] Evidence for the existence of two neutrinos has been obtained from the recent neutrino experiments.[6] The present theory is on firm ground provided neutrinoless $\mu \to e$ processes remain unobserved. This paper describes a new attempt

to detect the $\mu \to e + \gamma$ decay using spark chambers and applying the fast timing techniques of an earlier experiment on the $\mu \to 3e$ decay. A description of the general spark chamber arrangement has already been given.[7,8]

II. EXPERIMENTAL METHOD

The apparatus was designed primarily to observe the simultaneous emission of an electron and a gamma ray from $\mu \to e + \gamma$ at 180° following the decay of a stopped π^+ meson, and to obtain an estimate of their energies. This was done with a spark chamber-scintillator arrangement and appropriate oscilloscope recording. The spark chambers had a large solid angle for detecting the decays and yet had sufficient angular resolution to distinguish $\mu \to e + \gamma$ events from most of the $\mu \to e + \gamma + \nu + \bar{\nu}$ events near 180°. The scintillators and oscilloscopes provided fast time resolution between the

[1] E. P. Hincks and B. Pontecorvo, Phys. Rev. **73**, 257 (1948); S. Frankel, W. Frati, J. Halpern, L. Holloway, W. Wales, and O. Chamberlain, Nuovo Cimento **27**, 894 (1963); S. Frankel, J. Halpern, L. Holloway, W. Wales, M. Yearian, O. Chamberlain, A. Lemonick, and F. M. Pipkin, Phys. Rev. Letters **8**, 123 (1962); D. Bartlett, S. Devons, and A. Sachs, *ibid.* **8**, 120 (1962). References to earlier works may be found in these papers.

[2] A. Babaev, M. Balats, V. Kaftanov, L. Landsberg, V. Lyubimov, and Yu. Obukhov, Zh. Eksperim. i Teor. Fiz. **42**, 1685 (1962) [translation: Soviet Phys.—JETP **15**, 1170 (1962)] and Zh. Eksperim. i Teor. Fiz. **43**, 1984 (1962) [translation: Soviet Phys.—JETP **16**, 1397 (1963)]; S. Frankel, W. Frati, J. Halpern, L. Holloway, W. Wales, F. Betz, and O. Chamberlain, Phys. Rev. **130**, 351 (1962); S. Parker and S. Penman, Nuovo Cimento **23**, 485 (1962). References to earlier works may be found in these papers.

[3] G. Conforto, M. Conversi, L. di Lella, G. Penso, C. Rubbia, and M. Toller, Nuovo Cimento **26**, 261 (1962).

[4] S. Ogawa, Progr. Theoret. Phys. (Kyoto) **15**, 487 (1956); J. Schwinger, Ann. Phys. (N. Y.) **2**, 407 (1957); R. P. Feynman and M. Gell-Mann, Phys. Rev. **109**, 193 (1958); E. C. G. Sudarshan and R. E. Marshak, Phys. Rev. **109**, 1860 (1958); J. J. Sakurai, Nuovo Cimento **7**, 649 (1958).

[5] I. Kawakami, Progr. Theoret. Phys. (Kyoto) **19**, 459 (1957); K. Nishijima, Phys. Rev. **108**, 907 (1957); B. Pontecorvo, Zh. Eksperim. i Teor. Fiz. **37**, 1751 (1959) [translation: Soviet Phys.—JETP **10**, 1236 (1960)].

[6] G. Danby, J. Gaillard, R. Goulianos, M. Lederman, N. Mistry, M. Schwartz, and J. Steinberger, Phys. Rev. Letters **9**, 36 (1962).
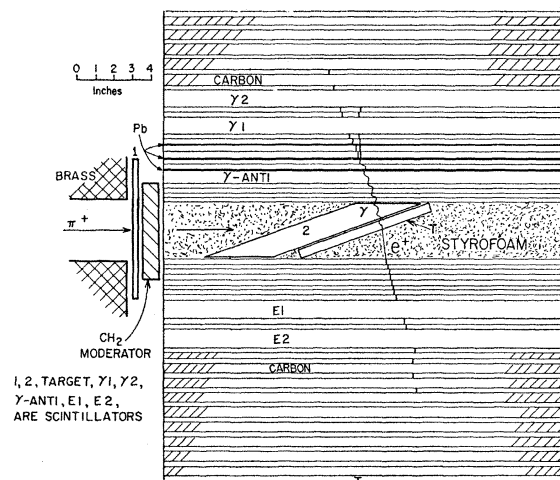
FIG. 1. Plan view of experimental setup.

[7] H. L. Anderson, *Nuclear Electronics* (International Atomic Energy Agency, Vienna, 1962), Vol. I, p. 263. The material in Ref. 8 supersedes that of Sec. III of this paper. See also H. L. Anderson, Rev. Sci. Instr. **32**, 510 (1961).

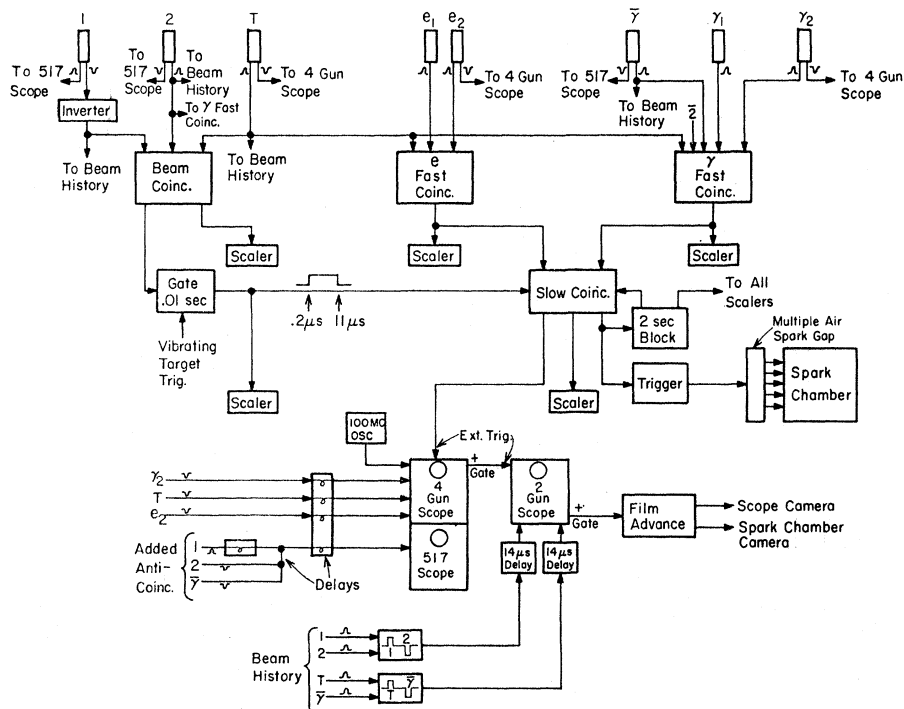[8] C. Rey and S. Parker, Nucl. Instr. and Methods **20**, 173 (1963).

FIG. 2. Simplified electronics block diagram.

electron and the gamma, and time information about the incoming beam. Lead plates were used to convert the gammas and carbon plates to measure the electron and positron ranges.

A 65-MeV π^+ beam from the vibrating target of the University of Chicago 460-MeV cyclotron was magnetically analyzed, directed through a 2-ft-thick lead wall, a brass collimator, a plastic scintillator (1) completely covering the exit, a polyethylene moderator, a final scintillator-moderator (2), and brought to a stop in a target (T) also made of plastic scintillator (see Fig. 1). Both 2 and T were slanted with their normals at 70° to the beam. This permitted the target to be thick in the direction of the beam (3.73 cm) and yet allowed decay electrons to leave it with a minimum of multiple Coulomb scattering. The moderator was similarly slanted so it could be placed close to the target.

The decay electrons were detected by scintillators (E_1 and E_2) in coincidence with T and in anticoincidence with 2. Information on the energy, direction, and timing of the electrons was obtained by the following array of 21-in.×21-in. elements (from T out): (1) eight spark chamber gaps ($E\zeta1-E\zeta8$), (2) 0.25-in. C (graphite density = 1.64 g/cc), (3) 0.375-in. scintillator (E_1), (4) 0.25-in. C, (5) two spark chamber gaps ($ES1,ES2$), (6) 0.25-in. C, (7) 0.375-in. scintillator (E_2), (8) 0.25-in. C, (9) one spark chamber gap [two sets ($ER1-ER2$) of (8) and (9)], (10) 0.5-in. C, (11) one spark chamber gap [eight sets ($ER3-ER10$) of (10) and (11)].

The direction of the electron was determined by the

first eight gaps and the energy by the last twelve. All gaps used in the experiment were 21-in.×21-in.×$\frac{1}{4}$-in. and were made with 0.012-in. Al plates.

Similar information for the gamma ray was obtained from the following array placed on the side of the target opposite the electron detectors: (1) four spark chamber gaps ($\gamma B1-\gamma B4$), (2) 0.375-in. scintillator ($\bar\gamma$), (3) 0.012-in. steel+0.062-in. lead+0.012-in. steel, (4) two spark chamber gaps [three sets ($\gamma C1-\gamma C6$) of (3) and (4)], (5) 0.375-in. scintillator (γ_1), (6) 0.25-in. carbon, (7) two spark chamber gaps ($\gamma S1-\gamma S2$), (8) 0.375-in. scintillator (γ_2), (9) 0.5-in. carbon, (10) one spark chamber gap [six sets ($\gamma R1-\gamma R6$) of (9) and (10)].

The first four gaps were used as anticoincidence gaps; the next six were used to determine the conversion point
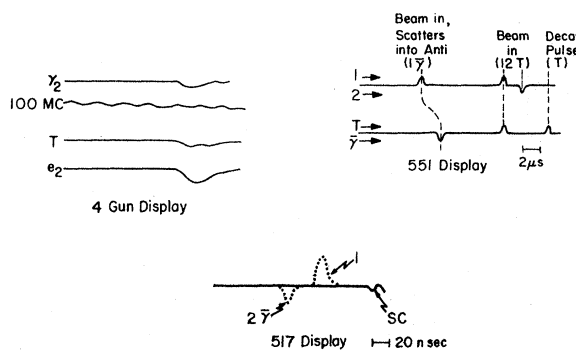

FIG. 3. Oscilloscope display. SC indicates start of spark chamber hash on 517.
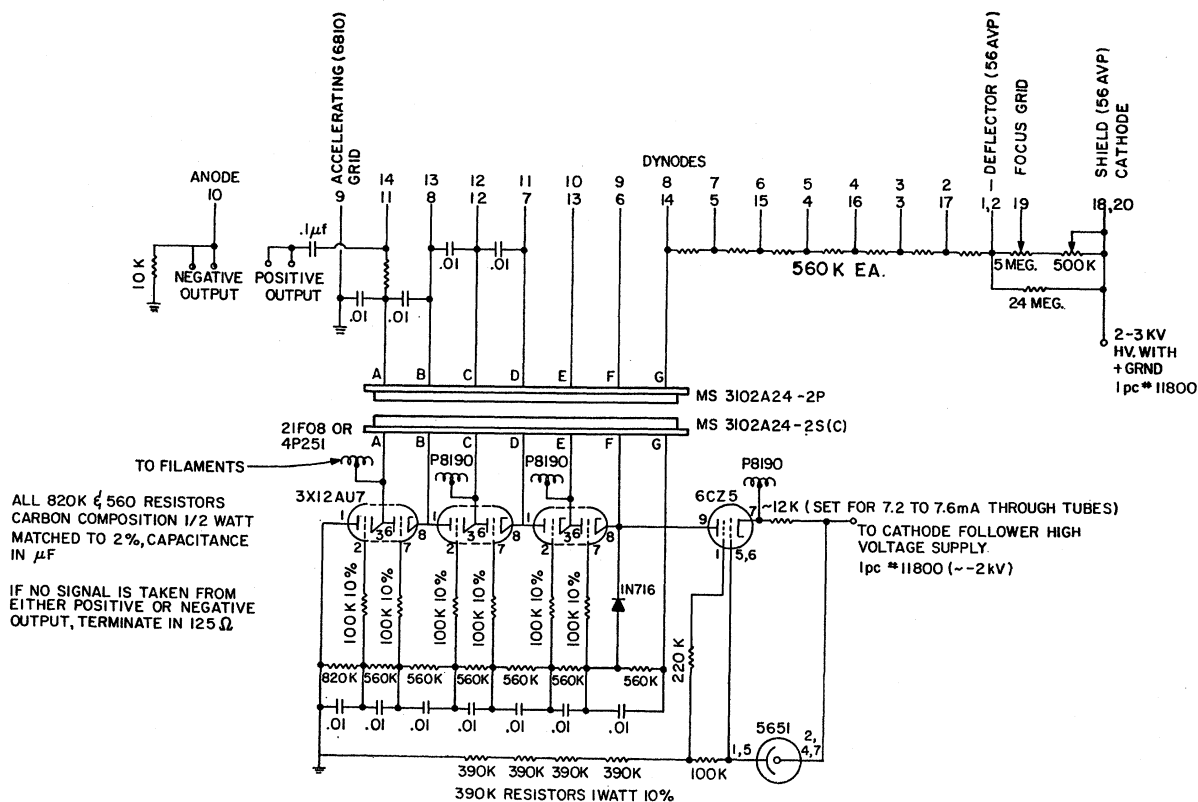
FIG. 4. Cathode follower tube base diagram.

of the gamma ray and estimate its direction; and the last eight were used to estimate its energy.

Details of the construction of the spark chamber modules, and the gas, optical, and pulsing systems have been given in a separate report.[8]

III. ELECTRONICS

A simplified block diagram of the electronics is shown in Fig. 2. A $12T$ coincidence during the long spill (0.01 sec) of the beam gated on a slow (50 nsec) coin-
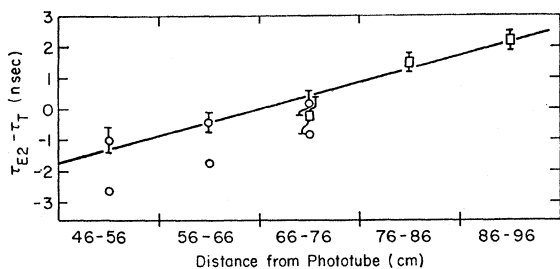
FIG. 5. Change in light collection time in plastic scintillator as a function of distance from the phototube. The flagged circles are for cosmic rays going *from* the upper part of the large scintillator (E_2) *to* the target. Twice the particle transit time has been added to the directly measured time differences (unflagged circles) for comparison with times for cosmic rays going *from* the target *to* the lower part of E_2 (squares).

cidence circuit from 0.2 to 11 μsec after the "$12T$" (0.2 to 6 μsec during the first part of the run). TE_1E_2 and $\bar{2}\bar{\gamma}\gamma_1\gamma_2$ coincidences in two moderately fast (15 nsec) circuits produced pulses which triggered the slow coincidence. This in turn triggered the scopes and spark chamber pulser.

Counter 2 was used in anticoincidence primarily to eliminate triggers from decay electrons originating in 2 and going through T, E_1, and E_2. Many of these will have passed through enough material to have scattered 5 to 10° before reaching the electron angle section.

Three scopes were used and photographed simultaneously: a four-beam fast scope,[9] a two-beam Tektronix 551, and a Tektronix 517 (see Fig. 3). Signals were taken from the anodes of the $56AVP$'s viewing scintillators γ_2, T, and E_2 to the deflection plates of the four-beam scope. Displaying the pulses on separate traces permitted arranging delays so that all the pulses arrived at the same time. As a result, sweep speed variations were less important than in the usual serial display. A fourth trace carried a 100-Mc/sec signal to eliminate any possible remaining error from this source.

A special cathode follower high-voltage supply was necessary to achieve a gain high enough to produce 15-

[9] H. G. Jackson, Rev. Sci. Instr. 29, 527 (1958); S. Penman, ibid. 32, 360 (1961).

to 30-V signals (0.5- to 1.0-cm deflection) at the scope input, since the large scintillators have a necessarily low light collection efficiency.[10] These high gains tend to produce a Stump-Talley type of instability[11] unless the supply has a low dynamic output impedance. The circuit is a modification of one designed by Penman[12] and is shown in Fig. 4.

In using large scintillators, one important correction that must be made is for variations in the light transit time through the scintillator. After timing approximately, using only the electronics, the apparatus was triggered on cosmic rays, and both the scope and spark chamber were photographed. Pulse times were measured by extrapolating the linear rise back to the baseline. The average time differences were plotted as a function of position in the scintillator. The time shift was a linear function of distance from the phototube with an effective velocity of (12.0±0.8) cm/nsec. One such plot is shown in Fig. 5. When this shift was used to correct individual events, the full width of the timing curve was reduced by a factor of two to 2.2 nsec for 50% of the cosmic ray events and 5.6 nsec for 90%. The remaining time spread is probably due to photoelectron collection time fluctuations in the phototubes since the low light collection efficiency (1.4%) from the large scintillators limits the number of photoelectrons.

The 551 display yielded information about the previous history of the beam. Pulses from counters 1, 2, T, and $\bar\gamma$ were shaped, sent through 14 μsec of Columbia HH2000 delay cable, and displayed. An additional separation of 1.5 μsec between 1 and 2 and between T and $\bar\gamma$ was provided by similar delay cable in the shaping circuit to space coincident pulses on the two traces. The pulse pair resolution time of the shapers was about 100 nsec. The rise time of the delay cable was about 500 nsec but two pulses occurring within the rise time of the cable clearly appeared as a larger pulse.

The 517 trace was used as a high gain, moderately fast display for the anticoincidence signals; a negative sum signal from 2 and $\bar\gamma$ and a positive signal from 1 delayed an additional 50 nsec. The anticoincidence thresholds on the electronics were set so that the circuits would still fire if small anti pulses were present. This enabled the thresholds to be set after the collection of data, to give the maximum anticoincidence efficiency possible consistent with negligible losses of valid events due to noise and after pulses in the phototubes.

A broad time resolution was used on the triggering coincidence circuits to permit simultaneous measurement of accidentals. This cannot be done by scaling counts from an additional coincidence circuit with one input delayed, since only a small fraction of out of time events produce acceptable spark chamber pictures. To reduce the number of spurious events photographed,

most of the data were taken with T required in the fast gamma coincidence circuit. Since almost all accidentals were due to on time TE_1E_2 events in accidental coincidence with on time $\bar{2}\bar\gamma\gamma_1\gamma_2$ events, this effectively reduced the width of the slow circuit to that of the fast ones. A plot of the time distribution of events with acceptable spark chamber pictures, taken with broad triggering time resolution is shown in Fig. 6(a). To improve the statistics of the plot, events with an electron-gamma angle and electron range outside the final acceptance criteria were included. This should not change the shape of the timing curve.

The two fast scope traces were completed before the noise from the spark chamber pulse reached them. The delay cable leading to the slow traces had its outer conductor grounded at both ends and was completely shielded, with the shield kept $\frac{1}{2}$ in. or more from the cable to prevent degradation of its rise time. With additional shielding and grounding of the scope, all but the first 4 μsec of the slow traces were usable.

IV. CRITERIA FOR EVENTS

The following were the criteria for the acceptance of events:

(1) One and only one track that projects back to the target, goes through the E section to $ER1$ or beyond, and does not stop at the end of a beam track.

(2) A track, or tracks that start from one point in one of the lead plates and go to $\gamma S2$ or beyond. This track must not have a γB section track leading to it,
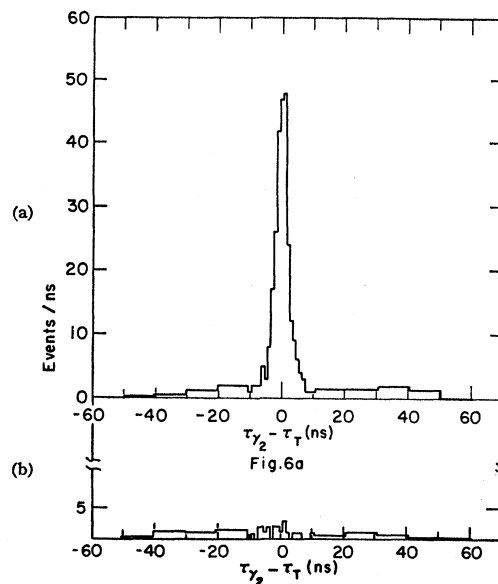

FIG. 6. (a) Number of events as a function of $\tau_{\gamma 2} - \tau_T$ (corrected for light collection time). Events outside central 20 nsec shown in 10 nsec groups. (b) Number of background events with tracks from the front of the chamber or γB section, or with "conversion" angle greater than 90° as a function of $\tau_{\gamma 2} - \tau_T$ (corrected for light collection time).

[10] R. L. Garwin, Rev. Sci. Instr. 23, 755 (1952).
[11] R. Stump and E. Talley, Rev. Sci. Instr. 25, 1132 (1954).
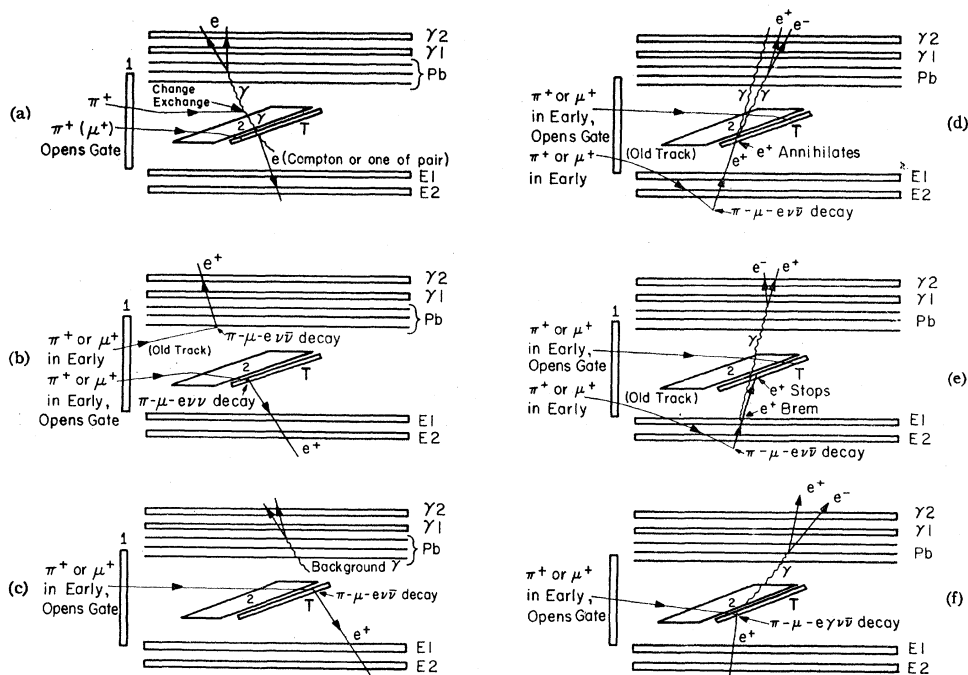[12] S. Penman, Rev. Sci. Instr. 30, 745 (1959).

Fig. 7. Sources of background.

and must not come from the front wall of the spark chamber.

(3) $\cos\theta_{e\gamma} \geq 0.98$, where $\theta_{e\gamma} = \pi - \cos^{-1}(\hat{p}_e \cdot \hat{p}_\gamma)$.

(4) Angle between γ and longest range conversion electron $\leq 80°$.

(5) Signals from T, E_2, and γ_2 within 8 nsec of each other after correction for light transit time. This rather broad criterion allows a high efficiency for on-time events and can be used because of the low accidental level.

(6) No scintillator pulses at prompt time from 1, 2, or $\bar{\gamma}$.

Strict range and angle criteria were not needed at this stage since the maximum likelihood method was used to analyze the data.

V. BACKGROUND

The high pion beam rate (20 000/sec) which was available during most of the run had the effect of keeping the gate open an appreciable fraction of the time. Accordingly, many of the events recorded were of accidental origin. The following types of spurious events were identified:

(1) pion charge exchange [see Fig. 7(a)]
(a) a beam particle traverses 1, 2, and T opening the gate,
(b) π^+ enters and charge exchanges to a π^0 ahead of 2,
(c) $\pi^0 \rightarrow \gamma + \gamma$;
(d) $\gamma \rightarrow e^-$ or $e^- + e^+$ in T (Compton or pair) and the electron enters E_1 and E_2;

(e) the other γ enters the lead converter and is detected.

This source of background was eliminated by rejecting events with prompt signals in 1. For the first part of the run, this signal was displayed only on a slow (551) trace. Events with 1 pulses within ±0.5 mm (±100 nsec) of the decay time position were rejected. This caused a 6% loss of effective "on time" for that part of the run because of accidental 1 pulses. No significant loss of this sort occurred after 1 was placed on a fast trace.

(2) $\pi - \mu - e$ on γ side [see Fig. 7(b)]

(a) π^+ (or μ^+) scatters from beam, stops in lead converter, and decays to μ^+,

(b) another π^+ (or μ^+) enters, stops in T, and decays to μ^+,

(c) $\mu^+ \rightarrow e^+ + \nu + \bar{\nu}$ in lead, e^+ enters γ_1 and γ_2 within the experimental time resolution,

(d) $\mu^+ \rightarrow e^+ + \nu + \bar{\nu}$ in T, e^+ enters E_1 and E_2 within the experimental time resolution.

(3) background γ [see Fig. 7(c)]

(a) π^+ (or μ^+) enters, stops in T, and decays to μ^+,

(b) $\mu^+ \rightarrow e^+ + \nu + \bar{\nu}$ in T, e^+ enters E_1 and E_2 within the experimental time resolution,

(c) γ, produced somewhere in or around spark chamber, converts and is detected in γ_1 and γ_2 within the experimental time resolution.

The second and third sources of background were

TABLE I. Spark midpoint to track deviations in projected views (mm in chamber space).

$\theta =$	0°–25°	25°–45°	45°–65°
"a" 50% less than	0.2	0.3	0.3
90% less than	0.5	1.0	0.9
"b" 50% less than	0.2	0.3	0.5
90% less than	0.5	1.2	1.6

reduced by rejecting events in which any of the following occurred:

(a) The track in the gamma section came from the entrance wall of the chamber.

(b) A track (usually almost parallel to the beam) in the γB section ended at the point of origin of the gamma section track.

(c) The angle between the gamma section track and the gamma was greater than 80°. (More than 99% of the time, the longest range conversion electron from a 53-MeV gamma will emerge from the lead at an angle of less than 80°.)

Background events with these characteristics also occurred out of time with equal probability. A plot of number versus electron-gamma time difference is shown in Fig. 6(b). The absence of a bump at zero time difference shows that the use of these criteria introduced no loss of efficiency for true coincidences. Events of these two types not eliminated by these criteria comprised the time accidental background. All but a negligible fraction of these were accidentals between coincident gamma side counts (γ_1, γ_2) and coincident electron side counts (TE_1E_2). As can be seen from Fig. 6(a), only 8% of the on-time events were accidentals.

(4) $\pi\mu e$ in electron side [see Fig. 7(d) and 7(e)]

(a) a beam particle traverses 1, 2, and T, opening the gate,

(b) a π^+ (or μ^+) enters and scatters into the carbon plates or final scintillator of the electron range section,

(c) $\pi^+ \rightarrow \mu^+ + \nu$, $\mu^+ \rightarrow e^+ + \nu + \bar{\nu}$,

(d) e^+ heads back toward the target,

(e) e^+ undergoes bremsstrahlung and stops in the target or

(e') e^+ annihilates in the target,

(f) resulting γ is detected on γ side.

This gave a prompt coincidence in E_2, E_1, T, γ_1, and γ_2 with no pulse in 2 and $\bar{\gamma}$, just the signature of a real event. In addition it produced events with a $\theta_{e\gamma}$ distribution peaked at 0°. Half of the observed angles were less than 7° and all of them were less than 15°.

This type of background was eliminated in part by rejecting all events which showed a track from the beam (either a π^+ or μ^+) stopping in the E_2 scintillator or first few range sections at the "end" of the electron track. As the spark chamber was not sensitive to tracks

older than about one muon lifetime, a certain number still remained in the data. This number was determined by taking the observed events of this type and studying the time distribution of beam particles as determined by the past history display. To increase the statistical accuracy of this study, events in which the tracks reached E_2 only were included. For particles coming from the beam but missing 2 and T this display showed a number 1 pulse unaccompanied by a coincident 2 or T. As some beam particles did scatter out of 2 and T, the time of the most recent 12 or $12T$ was taken for these cases. The time plot showed the decay time of the muon for the first 2 μsec and then fell off more rapidly for times greater than the 2 μsec sensitive time of the spark chamber. The calculated fraction of missed background events/observed background events was 0.32.

We identified 8 $\pi\mu e$ events on the electron side which had passed all other selection criteria. Thus, the estimated fraction among 241 events accepted was $8 \times 0.32/241 = 1.1\%$. The fraction within the most important angular region, $\theta_{e\gamma} \leq 4.5°$, was 1.7%. These events have typically short positron ranges since the beam particles do not penetrate far into the range section making it quite unlikely that they could be confused with $\mu \rightarrow e + \gamma$ events.

About 90% of the accepted on time events were genuine radiative muon decay events [see Fig. 7(f)]

(a) π^+ (or μ^+) enters and stops in T,

(b) $\pi^+ \rightarrow \mu^+ + \nu$, $\mu^+ \rightarrow e^+ + \gamma + \nu + \bar{\nu}$.

The observation of the predicted number of these events with the proper angular and range distribution showed that the apparatus would have detected $\mu \rightarrow e + \gamma$ events if they were present. In the final result, it was this process that set the limit on the experimental results.

VI. MEASUREMENT OF EVENTS

Spark locations in the two stereo views were measured using the measuring facility in this laboratory.[13] A preliminary measurement of cosmic-ray tracks was made to determine the accuracy of the spark chambers. The deviations of the midpoints of pairs of sparks in adjacent gaps from the actual track (determined by a least-squares fit to at least 22 sparks) are given in Table I. (See also Fig. 8.) The quantity "a" is the better measure of the accuracy of the spark chamber in locating a track in space. It varies only slowly with angle. This is partly because the reading error (0.1 to 0.2 mm) is comparable to the intrinsic error, and partly because even this intrinsic error does not vary rapidly with angle. It would be expected to be of the form $\delta \sin\theta \cos\theta$ for all but the very largest angles. Here δ is determined by the fluctuation in the distance along the track to the outermost free electron successful in starting an avalanche, and $\sin\theta \cos\theta$ comes from the pro-
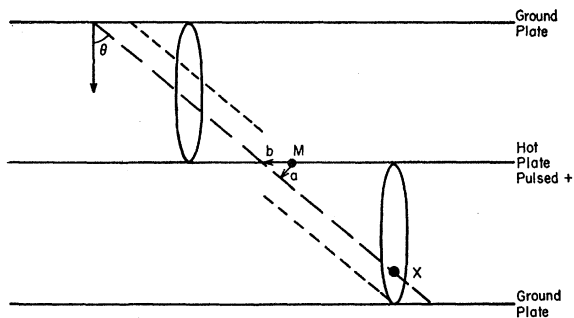
FIG. 8. Diagram of projected view of electron trail and sparks. Long dash, original electron trail; short dash, electron trail, shifted by clearing field; M, midpoint between outer sparks; a, deviation between M and original electron trail; b, deviation between M and intersection of original electron trail with central plate; X, intersection of original electron trail with spark.

jections of this fluctuation in forming "a." Our data are consistent with this description although the data certainly does not determine it uniquely.

The location of the electron and conversion electron tracks was determined from least-squares fits to the midpoints of pairs of sparks in adjacent gaps. Corrections of the order of 1% were made for optical distortions. If one of the two gaps missed, the point "X" was used (see Fig. 8). This point was 73% of the way from the hot to the ground plate and was determined from cosmic-ray data taken with the same clearing field (15 V) and delay times (300 nsec). The spark avalanches are usually started by one of the free electrons furthest from the midpoint since they have the longest path to the positive plate. When a single-ion trail produces more than one spark in a gap, the one furthest from the midpoint was used. The tracks thus determined were projected back to the center of the target and lead conversion plate, respectively. These two points then determined the gamma path.

The error in the electron-gamma angle was determined by using cosmic-ray muons as mock events, ignoring the sparks in the γB section. It was less than 0.7° for 50%, and 1.7° for 90% of the events. This is about 40% of the error due to multiple Coulomb scattering of the relatively soft electrons in the target and thus produces only an 8% increase in the rms error. Additional errors that are present in the conversion of a gamma, such as multiple Coulomb scattering in the lead, were small enough so that no appreciable broadening of the electron-gamma distribution was produced.

In calculating ranges, it was assumed the gamma converted in the middle of the lead plate before the first spark and the electrons stopped in the middle of the carbon plate after the last spark.

VII. CALCULATION OF EFFICIENCY

The detection efficiency for $\mu \rightarrow e + \gamma$ is the product of the following factors:

(1) The probability that the decay occurred while the

μ gate is open. This probability, including a small correction due to the gate being lengthened when two particles enter within 11 μsec, was 92.5%. (87% for the 6 μsec gate during the first part of the run.)

(2) The fractional solid angle subtended by γ_2 at the target, 24% of 4π.

(3) The probability that a $\mu \rightarrow e + \gamma$ decay would result in the electron passing through T, E_1, and E_2, and in the gamma converting in the lead and causing at least one charged particle to traverse γ_1 and γ_2. This is

$$\int_{\Omega_{\gamma_2}} P_e \mathcal{E}_\gamma \frac{d\Omega_{\gamma_2}}{4\pi} = \int_{\Omega_{\gamma_2}} P_e [\sum_{i=1}^{3} P_{\gamma i} C_\gamma (P_{+i} + P_{-i} - P_{+i} P_{-i})]$$

$$\times \frac{d\Omega_{\gamma_2}}{4\pi} = 4.7\%, \quad (1)$$

where P_e is the penetration probability of positron from T to $ER1$, ϵ_γ is the gamma detection efficiency, Ω_{γ_2} is the solid angle subtended by γ_2 at T (it is slightly less than Ω_{E_2}), $P_{\gamma i}$ is the penetration probability of a gamma to lead plate i, C_γ is the conversion probability of a gamma in one lead plate, P_{+i} is the penetration probability of a positron from lead plate i to γ_2, and P_{-i} is the penetration probability of an electron from lead plate i to γ_2.

$P_{\gamma i}$ and C_γ were determined from known gamma attenuation coefficients.[14] P_{+i} and P_{-i} were determined by using Wilson's Monte Carlo case histories of shower propagation to follow the converted electrons through the lead,[15] and tables of electron projected range straggling in carbon to determine the penetration probabilities of the electrons and positrons through the carbon to γ_2.[16] These straggling tables were also used to calculate P_e. The efficiency for 52.8-MeV γ's of the gamma side alone averaged over the available solid angle was 21%.

(4) Trigger efficiency. This was measured by triggering a dual beam scope on one scintillator signal and observing whether "on-time" signals from another scintillator placed on one trace were always accompanied by triggers. This was repeated for all combinations of input signals. The efficiency was essentially 100% except for the first part of the data where an error in timing reduced it to 94%.

(5) Four-gun scope display efficiency. The three signals on its traces were all larger than the required 1.5 V 100% of the time.

(6) Spark chamber efficiency. Due partly to the fact that multiple gaps were used in all crucial places, the efficiency for seeing an event was essentially 100%.

[14] G. Grodstein, Natl. Bur. Std. U. S. Circ. No. 583.

[15] R. R. Wilson, Phys. Rev. 86, 261 (1952), and private communication. The actual case histories were used in the efficiency calculation.

[16] J. Leiss, S. Penner, and C. Robinson, Phys. Rev. 107, 1544 (1957). The effects of annihilation were not included in this paper, but have been in our calculation.

(7) The probability that neither 1, 2, nor $\bar{\gamma}$ give an unrelated signal at the decay time. This probability was greater than 99% for all but the first part of the run when it was 94% due to 1 being only on a slow trace. This factor and the reductions in the gate and trigger efficiency during the first part of the run mentioned in point 4 have been applied to the number of beam stops during that part rather than the over-all efficiency.

(8) Multiple electron rejection factor. The probability that a picture including a valid decay had only one electron track between T, $E1$, and $E2$ was 90%. Accidentals, of course, will have a higher fraction of multiple tracks, and a small correction was made for this in calculating the factor. Events with more than one gamma conversion were rare and no correction to the efficiency was necessary.

(9) Scanning efficiency. One partial and two complete scans were made of the data. Comparing results gave a predicted scanning efficiency of 99.8%. The over-all efficiency thus was $0.925 \times 0.047 \times 1.00 \times 0.900 \times 0.998 = 0.039$.

VIII. EXPERIMENTAL RESULTS

The number of pions entering the target, including the correction mentioned in point 7 of Sec. VII was 1.21×10^{10}. The fraction of those that stopped, 0.61, was calculated from the observed ratio

number of $(\text{gate}_{12T}\ TE_1E_2)$

———————————————

number of $(12T)$

number of (muon decay electrons from T to E_2)

$= \dfrac{\qquad}{\text{number of (beam particles entering target)}}$,

the known gate delay and length (0.2 and 11 μsec), the solid angle subtended by E_2 at T ($0.28 \times 4\pi$), and the range distribution of muon electrons.

For a $\mu \to e + \gamma$ branching ratio of 10^{-8}, $1.21 \times 10^{10} \times 0.61 \times 0.039 \times 10^{-8} = 3$ events would have been seen. Of these 50% would have $\theta_{e\gamma} \le 1.8°$ and 90% would have $\theta_{e\gamma} \le 4.9°$.

Computer programs took the measured spark and fiducial coordinates, and where necessary, special coded instructions on spark selection for each event, made corrections for optical distortion, and calculated the electron range, the angles between the directions of the electron and the target normal, the electron and the gamma, and the gamma and the longest range member of the pair as it emerged from the lead.

241 events survived the selection criteria listed in Part IV. Their distribution in $\theta_{e\gamma}$ and electron range is shown in Fig. 9. Also shown are the calculated distributions for both $\mu \to e + \gamma$ and $\mu \to e + \gamma + \nu + \bar{\nu}$ of the electron-gamma angles $G_a(\theta_{e\gamma})$, $G_{a\nu}(\theta_{e\gamma})$ and the electron ranges $G_r(R_e)$, $G_{r\nu}(R_e)$.

The $\mu \to e + \gamma$ angular distribution G_a was calculated
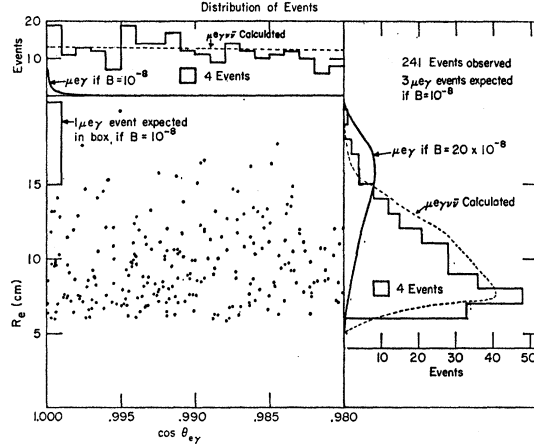

FIG. 9. Distribution in $\cos\theta_{e\gamma}$ and electron range of on time events.

for various path lengths of the electron in the target using the Molière theory for multiple Coulomb scattering. In the integration over the thickness of the target we assumed a uniform distribution of stopping pions. Since the actual distribution favored shorter path lengths, it is even more sharply peaked. The calculated distribution was widened by 8% to allow for measuring error. Separate tables were prepared for various groups of electron to target-normal angles to separate events with relatively wide and narrow distributions of $\theta_{e\gamma}$. The $\mu \to e + \gamma + \nu + \bar{\nu}$ angular distribution is almost constant over the range $0.98 \le \cos\theta_{e\gamma} \le 1$, with a small decrease in the detection efficiency away from 0° overcoming a small rise in the decay rate to produce a 4% drop from 1 to 0.98.

The positron range distribution, $P(E_e, R_e)$, was calculated using a Monte Carlo program that allowed for Landau straggling, bremsstrahlung, and annihilation, but not for scattering, thus giving the true, rather than the projected range.[17]

The observed range distributions then are

$$G_{r\nu}(R_e)dR_e = \int_{E_e} P(R_e, E_e) \int_{\cos\phi} T(R_e, E_e,\ \cos\phi)$$

$$\times \int_{E\gamma} B_\nu(E_e, E_\gamma)\epsilon_\gamma(E_\gamma,\ \cos\phi)$$

$$\times dE_\gamma d(\cos\phi)dE_e dR_e \quad (2)$$

and

$$G_r(R_e)dR_e$$

$$= BP(R_e, 52.8\ \text{MeV}) \int_{\cos\phi} T(R_e, 52.8\ \text{MeV},\ \cos\phi)$$

$$\times \epsilon_\gamma(52.8\ \text{MeV},\ \cos\phi)d(\cos\phi)dR_e, \quad (3)$$

where $T(R_e, E_e,\ \cos\phi) = $ penetration probability to $(ER1)$

————————————————

[17] S. Parker and C. Rey (to be published).

TABLE II. $10^7 \times$ differential branching ratio of $\mu \to e+\gamma+\nu+\bar{\nu}$ for $0.98 \le \cos\theta_{e\gamma} \le 1$ and E_e, E_γ in 5.3×5.3 MeV bins ($V-A$ theory).[a]

E_γ \ E_e	2.6	7.9	13.2	18.5	23.8	29.1	34.3	39.6	44.9	50.2
2.6	0.32	0.31	0.33	0.36	0.40	0.44	0.48	0.51	0.52	0.51
7.9	0.87	0.78	0.70	0.63	0.57	0.51	0.46	0.39	0.31	0.22
13.2	1.34	1.18	1.04	0.91	0.79	0.68	0.58	0.46	0.33	0.18
18.5	1.72	1.51	1.31	1.14	0.98	0.83	0.67	0.52	0.35	0.17
23.8	2.01	1.75	1.51	1.30	1.10	0.91	0.73	0.55	0.36	0.16
29.1	2.22	1.92	1.64	1.39	1.16	0.95	0.75	0.56	0.36	0.14
34.3	2.34	2.01	1.69	1.42	1.17	0.94	0.73	0.53	0.33	0.12
39.6	2.37	2.01	1.67	1.38	1.11	0.87	0.66	0.46	0.28	0.095
44.9	2.27	1.94	1.58	1.27	1.00	0.75	0.54	0.36	0.20	0.044
50.2	2.17	1.78	1.42	1.09	0.82	0.58	0.38	0.22	0.076	0.006

[a] See Ref. 18.

of a positron of energy E_e, true range R_e, and angle to the chamber normal ϕ; $B_\nu(E_e, E_\gamma) = $ differential branching ratio of $\mu \to e+\gamma+\nu+\bar{\nu}$ for $0.98 \le \cos\theta_{e\gamma} \le 1$ (see Table II)[18]; $B = $ branching ratio of $\mu \to e+\gamma$; and where the other symbols have been defined earlier. The estimated relative and absolute errors in the range distribution calculations are 10% to 15%.

The expected number of observed $\mu \to e+\gamma+\nu+\bar{\nu}$ events was found by integrating $G_{r\nu}dR_e$, multiplying by the number of stopped particles, the gate efficiency and the two electron rejection loss. The value found, 241, is in satisfactory agreement with the observed number remaining after background subtraction, 217.

IX. ANALYSIS

A. General

The usual method of analyzing experiments of this kind is to set acceptance limits on the relevant observables and to compare the probability of the outcome as calculated for various values of the branching ratio. In this case the useful observables were R_e and $\cos\theta_{e\gamma}$. The range information on the gamma side did not improve the discrimination between $\mu \to e+\gamma$ and background events and was not used in the analysis. The gamma side distributions for $\mu \to e+\gamma$ and $\mu \to e+\gamma+\nu+\bar{\nu}$ do not differ greatly and the accidentals, even though few in number, obscure this difference since a muon decaying in the lead to a 40- to 50-MeV electron often produces a long-range track. The limits were selected to exclude regions of large $\theta_{e\gamma}$ and small R_e which favor background to possible $\mu \to e+\gamma$ events, and which contribute little but statistical fluctuations to the analysis.

The expected number of background events in the interval $\bar{\nu}$ was determined by extrapolation from the interval $0.98 \le \cos\theta_{e\gamma} \le 0.997$. The events in this range constitute a fair sample of what can be expected within the acceptance limits, including the contribution from accidentals, and are substantially free of possible $\mu \to e+\gamma$ events.

[18] C. Fronsdal and H. Uberall, Phys. Rev. 113, 654 (1959); S. G. Eckstein and R. H. Pratt, Ann. Phys. (N. Y.) 8, 297 (1959). References to earlier works may be found in these papers.

B. Poisson Analysis

If the observed quantity is simply the number of events within the limits n then the Poisson formula

$$L(n, \bar{\gamma}+\bar{\nu}) = (1/n!)(\bar{\gamma}+\bar{\nu})^n \exp[-(\bar{\gamma}+\bar{\nu})] \quad (4)$$

gives the probability of seeing these n events (either background or $\mu \to e+\gamma$) where $\bar{\gamma}$ is the assumed average number of $\mu \to e+\gamma$ decays and $\bar{\nu}$ is the expected number of background events. The value of the $\mu \to e+\gamma$ branching ratio B corresponding to $\bar{\gamma}$ is

$$B = \bar{\gamma}/[(\text{no. stops})(\mu e\gamma \text{ detection efficiency})(\text{fraction of detected } \mu e\gamma \text{ within acceptance limits})] \quad (5)$$

$$= \frac{\bar{\gamma} \times 10^{-8}}{\bar{\gamma} \text{ expected for } B = 10^{-8}} \equiv \frac{\bar{\gamma} \times 10^{-8}}{\bar{\gamma}_e}.$$

TABLE III. Values of the assumed $\mu \to e+\gamma$ branching ratio B for which the probability of seeing the observed number of events falls to 50% and 10% of its value at $B = 0$.

$R_e \ge$	$\cos\theta_{e\gamma} \ge$	$\bar{\gamma}_e$	$\bar{\nu}$	n	B 50%	B 10%
12 cm	0.997	2.10	6.9	7	1.8×10^{-8}	3.5×10^{-8}
14	0.997	1.58	2.8	3	1.7	3.5
15	0.997	1.29	1.76	1	0.8	2.4
15	0.998	1.20	1.18	0	0.6	1.9
15	0.999	1.00	0.59	0	0.7	2.3

Our results give L its maximum value for $B \cong 0$.

Values of B for which L falls to 50% and 10% of its value at $B = 0$ and for several sets of limits are shown in Table III.

The results of some papers are given in terms of the value $\bar{\gamma}_m$ for which the integral

$$I(n, \bar{\gamma}_m, \bar{\nu}) = \int_0^{\bar{\gamma}_m} L(n, \bar{\gamma}+\bar{\nu})d\bar{\gamma} \Big/$$

$$\int_0^\infty L(n, \bar{\gamma}+\bar{\nu})d\bar{\gamma} = 0.90. \quad (6)$$

The value of B corresponding to $\bar{\gamma}_m$ is said to be the upper limit of the branching ratio to 90% confidence. It should be emphasized that I is not the probability that $\bar{\gamma}$ is less than $\bar{\gamma}_m$. For instance, even when no events are seen and $\bar{\gamma}=0$ clearly cannot be excluded, I becomes arbitrarily small as $\bar{\gamma}_m$ approaches zero.

The significance of I can be seen by noting that

$$\int x^n e^{-x} dx = -e^{-x} \sum_{i=0}^{n} x^i \frac{n!}{i!} + \text{const}$$

and

$$I(n, \bar{\gamma}_m, \bar{\nu}) = 1 - \sum_{i=0}^{n} L(i, \bar{\gamma}_m + \bar{\nu}) / \sum_{i=0}^{n} L(i, \bar{\nu}). \quad (7)$$

Thus the upper limit to 90% confidence is that value at which the probability of seeing the observed number or fewer events has dropped to 10% of its value for $\bar{\gamma}=0$.

C. Maximum Likelihood Analysis

In order to use more fully the available data on the values of $\cos\theta_{e\gamma}$ and R_e for each event, we calculate the probability of seeing the observed number of events with the observed distribution as a function of an assumed $\mu \to e+\gamma$ branching ratio.

The differential probability $f(\cos\theta_{e\gamma}, R_e; \bar{\gamma})$, for observing an event at $(\cos\theta_{e\gamma}, R_e)$ as a function of $\bar{\gamma}$ is

$$f(\cos\theta_{e\gamma}, R_e; \bar{\gamma}) d(\cos\theta_{e\gamma}) dR_e$$
$$= [\bar{\gamma} G_a(\cos\theta_{e\gamma}) G_\gamma(R_e) + \bar{\nu} G_{a\nu}(\cos\theta_{e\gamma}) G_{r\nu}(R_e)]$$
$$\times d(\cos\theta_{e\gamma}) dR_e. \quad (8)$$

The joint differential probability of seeing just n events at the observed values of $\cos\theta_{e\gamma i}, R_{e i}$ is called the likelihood function[19] and in the present case is given by

$$\mathcal{L}(n, \bar{\gamma})$$
$$= \exp\left[-\int_{(R_e)_{\min}}^{(R_e)_{\max}} \int_{0.997}^{1.000} f(\cos\theta_{e\gamma}, R_e; \bar{\gamma}) d(\cos\theta_{e\gamma}) dR_e \right]$$
$$\times \prod_{i=1}^{n} f(\cos\theta_{e\gamma i}, R_{e i}; \bar{\gamma}) \quad (9)$$

$$= \exp[-(\bar{\gamma} + \bar{\nu})] \prod_{i=1}^{n} f(\cos\theta_{e\gamma i}, R_{e i}; \bar{\gamma}),$$

where the term $\exp[-(\bar{\gamma}+\bar{\nu})]$ accounts for the absence of events at other than the indicated points. All the G's are normalized to unity over the selected intervals. In our case, the interval $0.997 \leq \cos\theta_{e\gamma} \leq 1.000$ seemed a good choice since 93% of the $\mu \to e+\gamma$ events should occur within it and the remaining interval $0.98 \leq \cos\theta_{e\gamma} \leq 0.997$ is large enough to establish the value of $\bar{\nu}$ and the G's for the background events.

Plots of $\mathcal{L}$ as a function of B, normalized to unity

[19] J. Orear, University of California, Lawrence Radiation Laboratory Report No. UCRL 8417 (unpublished); F. Solmitz, Institute for Nuclear Studies, University of Chicago (unpublished).
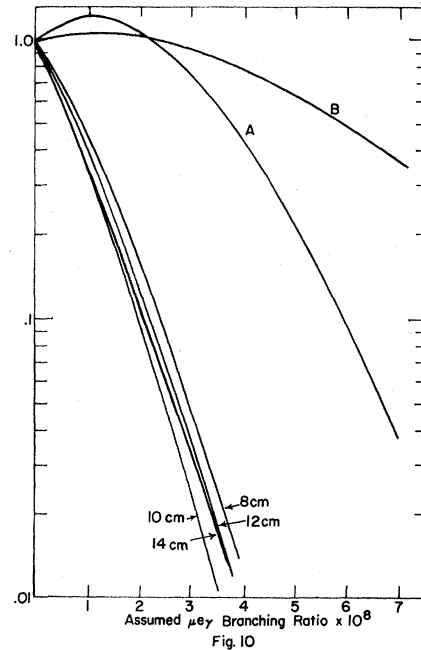

Assumed $\mu e\gamma$ Branching Ratio $\times 10^8$

Fig. 10

FIG. 10. Relative likelihood function for observed results as a function of assumed $\mu \to e+\gamma$ branching ratio for positron range lower limits of 8, 10, 12, and 14 cm of graphite. Also shown are the relative probabilities for seeing the results of Frankel et al. (1963) (curve A) and Bartlett, Devons, and Sachs (1962) (curve B). Curve A is the derivative of the solid curve in Fig. 10 of Frankel et al.

at $B=0$, are shown in Fig. 10 for various values of $(R_e)_{\min}$. The value of $(R_e)_{\max}$ was fixed at 20 cm, somewhat beyond the limit expected for $\mu \to e+\gamma$ positrons. In all cases $\mathcal{L}$ reaches its largest value at $B=0$. Table IV displays the pertinent parameters for each value of R_e chosen and the values of B for which $\mathcal{L}$ drops to 50% and 10% of its value for $B=0$. The results are rather independent of the choice of $(R_e)_{\min}$. It is clear that our experiment is consistent with $B=0$ while the sensitivity of our measurement is expressed by the values of B for which the probability of observing the set of events found by us has fallen to either 50% or 10% of its value at $B=0$.

Figure 10 also includes plots of the Poisson term L

TABLE IV. Values of the assumed $\mu \to e+\gamma$ branching ratio B for which the probability of seeing the observed number of events and the observed distribution in R_e and $\cos\theta_{e\gamma}$ falls to 50% and 10% of its value at $B=0$.

$R_e \geq$	$\cos\theta_{e\gamma} \geq$	$\bar{\gamma}$ expected for $B=10^{-8}$	$\bar{\nu}$	n	B 50%	B 10%
8 cm	0.997	2.57	24.2	22	0.89×10^{-8}	2.38×10^{-8}
10	0.997	2.39	14.8	11	0.66	1.95
12	0.997	2.10	6.9	7	0.76	2.19
14	0.997	1.58	2.8	3	0.68	2.08

calculated from the corresponding values of $\bar{\gamma}_o$, $\bar{\nu}$, and n as deduced from the two latest experiments.[1]

X. CONCLUSIONS

The results of the experiment have been analyzed by expressing the probability of seeing the observed data as a function of the assumed $\mu \to e + \gamma$ branching ratio B. Limits on the electron range and electron-gamma angle have been used in the selection of events to exclude regions strongly favoring $\mu \to e + \gamma + \nu + \bar{\nu}$ over $\mu \to e + \gamma$. Once events with the shortest range electrons have been excluded, the results are substantially independent of the exact choice of limits. The probability is largest for $B = 0$, drops to less than 50% of this value for $B = 0.8 \times 10^{-8}$, and to less than 10% of this value for $B = 2.2 \times 10^{-8}$.

The results of this and the two preceding experiments could be combined by multiplication of the three probability distributions. However, this joint probability is not significantly lower for $B \leq 2 \times 10^{-8}$ and thus does not change the above results appreciably.

Uncrossed Ladder Graphs in the Feinberg-Pais Theory of Leptonic Weak Interactions

Yih Pwu[†]

University of Pennsylvania, Philadelphia, Pennsylvania

AND

Tai Tsun Wu[*]

Institute for Advanced Study, Princeton, New Jersey

(Received 23 July 1963)

The Feinberg-Pais theory of summing the uncrossed ladder graphs is re-examined. A single regularization of the W propagator is used throughout. Instead of the iterative procedure used previously, the leading terms of the individual graphs are summed exactly. The result of Feinberg and Pais for energies much below 300 BeV is obtained for all energies in the limit of infinite regulator mass.

1. INTRODUCTION

RECENTLY, Feinberg and Pais[1] studied the higher order effects in weak interactions. In their work, the weak interactions are assumed to be mediated by massive bosons W of spin 1, and neutral lepton currents are assumed to be absent in the Lagrangian. In studying two-body scattering processes involving only leptons, Feinberg and Pais restricted their consideration of higher order weak interactions to the uncrossed ladder graphs only. The rungs of these graphs consist alternatively of W^+ and W^-, a fact of great importance in their work. So far as leptonic weak interactions are concerned, one of the important conclusions of Feinberg and Pais is that, for the so-called allowed processes, the

factor

$$-i(\delta_{\mu\nu} + m^{-2} q_\mu q_\nu)/(q^2 + m^2) \qquad (1.1)$$

in the expression for the matrix element should be replaced, when higher order effects are taken into account, by

$$-i\tfrac{3}{4}[\delta_{\mu\nu}(1 - \tfrac{1}{3} m^{-2} q^2) + \tfrac{4}{3} m^{-2} q_\mu q_\nu]/(q^2 + m^2) \qquad (1.2)$$

provided that q satisfies

$$|q^2 g^2 / m^2| \ll 1. \qquad (1.3)$$

Here m denotes the mass of W, and g is the W-lepton coupling constant.

It is the purpose of this paper to study in more detail the properties of these uncrossed ladder graphs. We do not inquire into the effects of more complicated graphs; instead, given these uncrossed ladder graphs and some rules of computation to be outlined in Sec. 2, we ask what mathematical deductions are possible. Since it

[1] G. Feinberg and A. Pais, Phys. Rev. 131, 2724 (1963).